

# A near-global climatology of oceanic coherent eddies

Josué Martínez-Moreno<sup>1</sup>, Andrew McC. Hogg<sup>1</sup>, and Matthew H. England<sup>2</sup>

<sup>1</sup>Research School of Earth Science and ARC Center of Excellence for Climate Extremes, Australian National University, Canberra, Australia

<sup>2</sup>Climate Change Research Centre (CCRC), UNSW Australia, Sydney NSW, Australia

## Key Points:

- Coherent eddies contain around 50% of the total surface ocean kinetic energy budget.
- Seasonal cycle of the number of coherent eddies and the coherent eddy amplitude reveals a 3-6 month lag to wind forcing.
- The seasonal lag between the number and the amplitude of coherent eddies suggests a role for the inverse cascade.

**13 Abstract**

14 Ocean eddies influence regional and global climate through mixing and transport of heat  
15 and properties. One of the most recognizable and ubiquitous feature of oceanic eddies  
16 are coherent vortices with spatial scales of tens to hundreds of kilometers, frequently re-  
17 ferred as “mesoscale eddies”. Coherent mesoscale eddies are known to transport prop-  
18 erties across the ocean and to locally affect near-surface wind, cloud properties, and rain-  
19 fall patterns. Although coherent eddies are ubiquitous, their climatology, seasonality, and  
20 long-term temporal evolution remains poorly understood. Here, we examine the kinetic  
21 energy contained by coherent eddies and present the seasonal, interannual and long-term  
22 variability using satellite observations between 1993 to 2019. A total of  $\sim$ 37 million co-  
23 herent eddies are detected in this analysis. Around 50% of the kinetic energy contained  
24 by ocean eddies corresponds to coherent eddies. Additionally, a strong seasonal cycle is  
25 observed, with a 3–6 months lag between the wind forcing and the response of the co-  
26 herent eddy field. The seasonality of the number of coherent eddies and their amplitude  
27 reveals that the number of coherent eddies responds faster to the forcing ( $\sim$ 3 months),  
28 than the coherent eddy amplitude (which lags by  $\sim$ 6 months). This seasonal cycle is spa-  
29 tially variable, so we also analyze their climatology in key oceanic regions. Our analy-  
30 sis highlights the relative importance of the coherent eddy field in the ocean kinetic en-  
31 ergy budget, implies a strong response of the eddy number and eddy amplitude to forc-  
32 ing at different time-scales, and showcases the seasonality, and multidecadal trends of  
33 coherent eddy properties.

**34 Plain language summary**

35 Coherent eddies are the most common feature of ocean variability observable from  
36 satellites. They are crucial in ocean dynamics as they can transport properties over long  
37 distances and interact with the atmosphere. Our study investigates the seasonal, inter-  
38 annual, and long-term changes in the abundance and intensity of coherent eddies, by au-  
39 tomatically identifying individual eddies over the available satellite altimeter record. The  
40 seasonal cycle suggests a transition from numerous, smaller, and weaker coherent eddies,  
41 to fewer and larger, and stronger coherent eddies over the season. In addition, a long-  
42 term adjustment of the coherent eddy field is identified with possible links to long-term  
43 changes in the climate system.

## 44 1 Introduction

45 Mesoscale ocean variability with spatial scales of tens to hundreds of kilometers is  
 46 comprised of processes such as vortices, waves, and jets (Ferrari & Wunsch, 2009; Fu et  
 47 al., 2010). These mesoscale processes are highly energetic, and they play a crucial role  
 48 in the transport of heat, salt, momentum, and other tracers through the ocean (Wun-  
 49 sch & Ferrari, 2004; Wyrtki et al., 1976; Gill et al., 1974). One of the most recognizable  
 50 and abundant ocean processes observable from space are mesoscale vortices. Although  
 51 mesoscale vortices are commonly referred to in the literature as “mesoscale eddies”, this  
 52 term is also often used to describe the total mesoscale ocean variability (the time-varying  
 53 component of the mesoscale flow), thus, to avoid ambiguity we will refer to mesoscale  
 54 vortices as *coherent eddies*. Coherent eddies are abundant and energetic; they are essen-  
 55 tial to ocean dynamics as concluded by many previous studies (Hogg & Blundell, 2006;  
 56 Siegel et al., 2011; Beron-Vera et al., 2013; Frenger et al., 2013, 2015; Pilo et al., 2015;  
 57 Schubert et al., 2019; Patel et al., 2020).

58 Coherent eddies are quasi-circular geostrophic currents. According to their rota-  
 59 tional direction and the sign of the Coriolis parameter, the sea surface height anomaly  
 60 within a coherent eddy can have a negative or positive sea surface height anomaly (cold-  
 61 core and warm-core coherent eddies, respectively). This characteristic sea surface height  
 62 signature of coherent eddies has been utilized to identify and track coherent eddies from  
 63 satellite altimetry (e.g., Chelton et al., 2007; Faghmous et al., 2015; Ashkezari et al., 2016;  
 64 Martínez-Moreno et al., 2019; Cui et al., 2020). Automated identification algorithms of  
 65 coherent eddies have revealed their ubiquity in the oceans, with a predominant influence  
 66 at hotspots of eddy activity such as in boundary current extensions and the Antarctic  
 67 Circumpolar Current. In these regions, it has been estimated that coherent eddies con-  
 68 tribute around 40–50% of the net mesoscale kinetic energy (Chelton et al., 2011) and thus  
 69 a significant fraction of the total kinetic energy (Ferrari & Wunsch, 2009). Although this  
 70 estimate showcases the importance of the mesoscale coherent eddy field, the energy con-  
 71 tained by coherent eddies was estimated by extracting the total geostrophic velocity within  
 72 the radius of each detected coherent eddy; thus, it is possible that this estimate may con-  
 73 tain energy from other processes. Here we extend on this past work by reconstructing  
 74 the surface imprint of coherent eddies using a new eddy tracking algorithm and using  
 75 the latest available satellite record.

76 There is broad consensus that mesoscale eddy kinetic energy has a pronounced sea-  
77 sonal variability (Qiu, 1999; Qiu & Chen, 2004; Kang & Curchitser, 2017; Uchida et al.,  
78 2017). Several hypotheses have been proposed to explain this seasonality including: sea-  
79 sonal variations of atmospheric forcing (Sasaki et al., 2014), seasonality of the mixed layer  
80 depth (Qiu et al., 2014; Callies et al., 2015), seasonality of the intensity of barotropic in-  
81 stability (Qiu & Chen, 2004), the variability of the baroclinic instability due to the sea-  
82 sonality of the vertical shear (Qiu, 1999), and a seasonal lag of the inverse energy cas-  
83 cade (i.e. energy is transported between scales, from small to large; Arbic et al., 2013)  
84 in combination with the presence of a front in the mixed layer, which can lead to a sea-  
85 sonal cycle of the baroclinic instability (Qiu et al., 2014). On one hand, processes such  
86 as barotropic and baroclinic instabilities control the seasonality of coherent eddies in the  
87 ocean. On the other hand, recent studies using observations and eddy-permitting climate  
88 models suggest slower adjustments of the global ocean that create long-term changes in  
89 the coherent eddy field. Such readjustments include a multidecadal increase in the ocean  
90 stratification resulting from temperature and salinity changes (Li et al., 2020), a hori-  
91 zontal readjustment of sea surface temperature gradients (Cane et al., 1997; Bouali et  
92 al., 2017; Ruela et al., 2020), and an intensification of the kinetic energy, eddy kinetic  
93 energy, and mesoscale eddy kinetic energy over the last 3 decades as a consequence of  
94 an increase in wind forcing (Hu et al., 2020; Wunsch, 2020; Martínez-Moreno et al., 2021).  
95 All of these seasonal factors and long-term readjustments directly influence the annual  
96 and decadal response of the coherent eddy field, however, the seasonality of the coher-  
97 ent component of the eddy kinetic energy, as well as the seasonal cycle and trends of the  
98 coherent eddy statistics, remain unknown.

99 Here we present a new global climatology of the coherent eddy kinetic energy by  
100 reconstructing the coherent eddy signature from satellite observations. Our study doc-  
101 uments the seasonal cycle of the coherent eddy kinetic energy, and the seasonal cycle and  
102 long-term trends of the coherent eddy properties over the satellite record. Moreover, we  
103 conduct more detailed analyses in regions where coherent eddies dominate the eddy ki-  
104 netic energy field. The rest of this paper is structured as follows: the data sources and  
105 methodology are described in Section 2. Then, we present the climatology, energy ra-  
106 tios, and global seasonality of the coherent eddy kinetic energy in Section 3. Section 4  
107 outlines the global climatology and seasonality of coherent eddy properties, followed by  
108 long-term changes of the coherent eddy properties (Section 5). Then we focus our at-

109 tention on the seasonal cycle and coherent eddy properties in regions dominated by co-  
 110 herent eddies (Section 6). Finally, Section 7 summarizes the main results and discusses  
 111 the implications of this study.

112 **2 Methods**

113 We use daily sea surface height (SSH) data made available by the Copernicus Ma-  
 114 rine Environment Monitoring Service in near real time (CMEMS, 2017). This gridded  
 115 product contains the sea surface height and geostrophic velocities with daily  $0.25^\circ$  res-  
 116 olution from January 1993 to 2019. The daily geostrophic velocities allow us to compute  
 117 the kinetic energy (KE) and eddy kinetic energy (EKE) over the satellite record. The  
 118 main source of EKE is the time-varying wind (Ferrari & Wunsch, 2009); thus, we also  
 119 compute the seasonal cycle of the wind magnitude from the JRA55 reanalysis (Japan  
 120 Meteorological Agency, Japan, 2013) using wind velocities at 10m above the ocean's sur-  
 121 face.

122 Over the same record, coherent eddy statistics from Martínez-Moreno et al. (2019),  
 123 hereafter MM19, are analyzed and compared with those released by Chelton & Schlax  
 124 (2013), hereafter CS13. Both datasets are gridded in a  $1^\circ$  resolution and are produced  
 125 via automated eddy identification algorithms using closed contours of SSH. However, these  
 126 datasets have important differences in the criteria they use to identify and record coher-  
 127 ent eddies statistics. The major differences include: (i) MM19's algorithm requires an  
 128 adjustment between a 2D Gaussian and the SSH anomaly (SSHa) surface within the iden-  
 129 tified closed contour, while CS13's only uses the outermost closed contour of SSH; (ii)  
 130 MM19's dataset reports the maximum SSHa within the identified coherent eddy, while  
 131 CS13's algorithm reports the maximum SSH value minus the discrete level in which the  
 132 coherent eddy was identified; and (iii) MM19's dataset includes all detected coherent ed-  
 133 dies, while CS13's dataset excludes coherent eddies with lifetimes shorter than four weeks  
 134 and coherent eddy amplitudes smaller than 1cm. Moreover, MM19's algorithm allows  
 135 the reconstruction of the coherent eddy field under the assumption that coherent eddies  
 136 have a 2D Gaussian imprint in the sea surface height. This Gaussian reconstruction of  
 137 the coherent eddy field then allows us to estimate the coherent geostrophic eddy veloc-  
 138 ities and thus the kinetic energy contained only by coherent eddies.

139            **2.1 Kinetic Energy decomposition**

140            Kinetic energy is commonly divided into the mean and time-varying components  
 141            through a Reynolds decomposition. At a given time, the surface velocity field  $\mathbf{u} = (u, v)$   
 142            is split into the time mean ( $\bar{\mathbf{u}}$ ) and time varying components ( $\mathbf{u}'$ ). Moreover, MM19 pro-  
 143            posed to further decompose the eddy kinetic energy into the energy contained by coher-  
 144            ent features ( $\mathbf{u}'_e$ ) and non-coherent features ( $\mathbf{u}'_n$ ). Therefore the KE equation can be writ-  
 145            ten as:

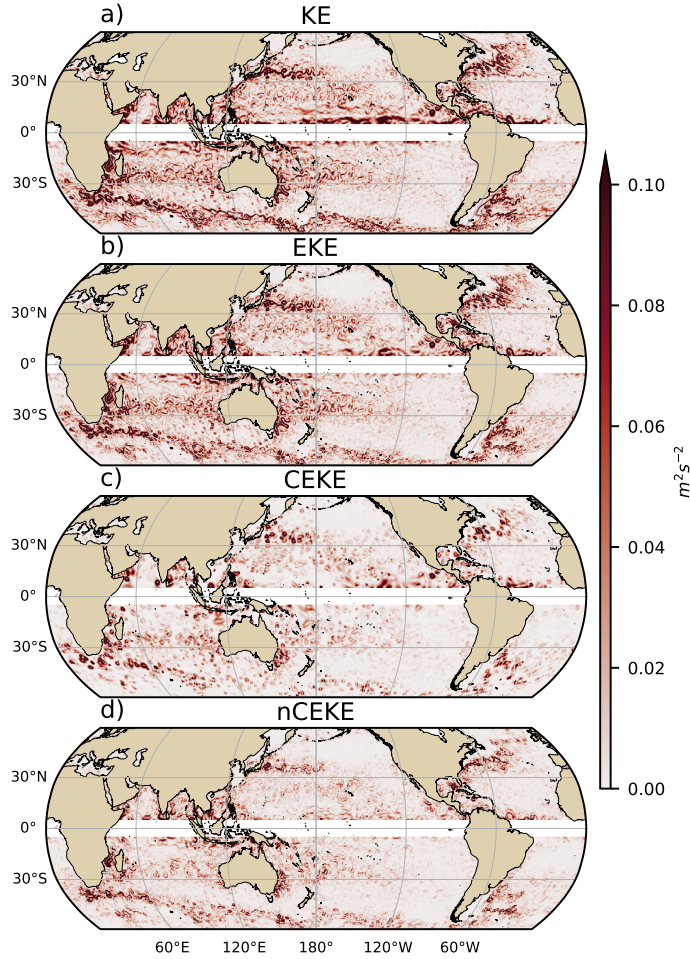
$$\text{KE} = \underbrace{\bar{u}^2 + \bar{v}^2}_{\text{MKE}} + \underbrace{u'^2_e + v'^2_e}_{\text{CEKE}} + \underbrace{u'^2_n + v'^2_n}_{\text{nCEKE}} + \mathcal{O}_c^2 + \mathcal{O}^2 \quad (1)$$

146            Due to the properties of this decomposition, the second order term  $\mathcal{O}^2$  is zero when  
 147            averaged over the same period as  $\bar{\mathbf{u}}$ . However,  $\mathcal{O}_c^2$  is not necessarily negligible, unless it  
 148            is averaged over time and space. More information about the decomposition of the field  
 149            into coherent features and non-coherent features is explained in Martínez-Moreno et al.  
 150            (2019). A global snapshot of each component of kinetic energy decomposition is shown  
 151            in Figure 1, where the KE and EKE are comprised of rings and filaments. As expected,  
 152            the decomposition of EKE into CEKE and nCEKE components exhibits only the ring-  
 153            like signatures expected of coherent eddies, while the non-coherent component primar-  
 154            ily shows filaments, with some mis-identified coherent eddies.

158            **2.2 Eddy statistics**

159            The eddy statistics used in this study include (i) the eddy count ( $cEddy_n$ ) defined  
 160            as the number of coherent eddies per grid cell, (ii) the eddy diameter defined as the di-  
 161            ameter of a circle with equal area to the closed contour of each identified eddy, and (iii)  
 162            the mean eddy amplitude defined as the mean amplitude of the coherent eddies within  
 163            the cell ( $cEddy_{amp}$ ). The latter metric can be separated into positive ( $cEddy_{amp}^+$ ) and  
 164            negative ( $cEddy_{amp}^-$ ) coherent eddy amplitudes, defined as the mean amplitude of warm  
 165            core and cold core coherent eddies, respectively, within the cell. The polarity indepen-  
 166            dent eddy amplitude ( $|cEddy_{amp}|$ ) is defined as:

$$|cEddy_{amp}| = \frac{1}{2} (cEddy_{amp}^+ - cEddy_{amp}^-) \quad (2)$$



155 **Figure 1.** Snapshot of surface kinetic energy ( $\overline{KE}$ ), surface eddy kinetic energy ( $\overline{EKE}$ ),  
 156 surface coherent eddy kinetic energy ( $\overline{CEKE}$ ), and surface non-coherent eddy kinetic energy  
 157 ( $\overline{nCEKE}$ ) for the 1st of January 2017.

167 Note that the  $cEddy_{amp}^+$  and  $cEddy_{amp}^-$  are sign definite, thus the difference will always  
 168 be positive, whereas the gridded averaged  $cEddy_{amp}$  can be negative or positive noting  
 169 the dominant polarity of coherent eddies in the region, and the absolute value of  $cEddy_{amp}$   
 170 is denoted by  $cEddy_{|amp|}$ . We analyze the climatology and trends of the above eddy statis-  
 171 tics over the available satellite record, namely between 1993 and 2019. We exclude the  
 172 equatorial region ( $10^\circ S - 10^\circ N$ ) and regions poleward of  $60^\circ$ , because the geostrophic ap-  
 173 proximation is invalid near the Equator and the satellite spatial coverage at high-latitudes  
 174 is unable to resolve the coherent eddy scales polewards of  $60^\circ$ . Note that the climatol-  
 175 ogy of  $cEddy_n$  is computed by adding all the identified eddies over the record, while all

other climatological statistics are computed as the time-average over the record. Seasonal climatologies are calculated for the monthly average of each coherent eddy statistic, while hemispheric time-series are filtered with a running average of 90 days. Trends of  $cEddy_n$  and  $|cEddy_{amp}|$  are calculated by coarsening the dataset to a  $5^\circ$  grid, and then linear trends are computed for each grid point. The statistical significance of trends is assessed by a modified Mann-Kendall test above the 95% confidence level (Yue & Wang, 2004).

Time averages are denoted by  $\overline{\phantom{x}}$ , while area-weighted averages are denoted using  $\langle \phantom{x} \rangle$ , where the area-weighted average of a function  $f$  is:

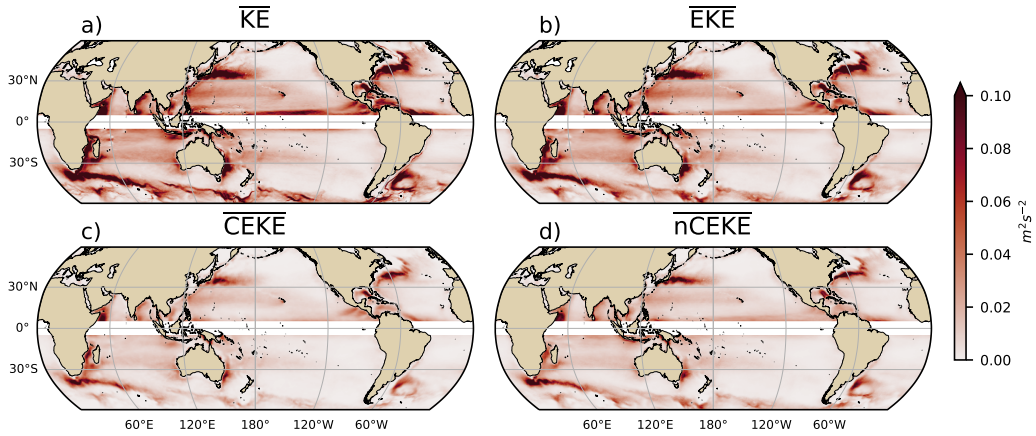
$$\langle f \rangle = \frac{\int f \xi dx dy}{\int \xi dx dy}, \quad (3)$$

where  $\xi$  is a mask that is set to zero in grid cells where no coherent eddies were identified and one elsewhere.

### 3 Global Coherent Eddy Energetics

The kinetic energy decomposition estimated from sea surface height measured by satellite altimeters averaged from 1993-2019 is shown in Figure 2. These maps show that many regions of the global ocean are highly energetic in mean KE ( $\overline{KE}$ ), mean EKE ( $\overline{EKE}$ ), mean coherent eddy kinetic energy ( $\overline{CEKE}$ ) and mean non-coherent eddy kinetic energy ( $\overline{nCEKE}$ ). The spatial pattern highlights well-known regions of the ocean where mesoscale processes are abundant, such as the western boundary current (WBC) extensions and the Antarctic Circumpolar Current. The spatial distribution of the energy contained by the reconstructed mesoscale coherent eddies and non-coherent components are similar (Figures 2c,d). However, there are some regions where coherent eddies dominate over non-coherent, and vice-versa. Overall, this decomposition suggests that boundary current extensions and other energetic regions of the ocean contain both coherent and non-coherent components of the kinetic energy.

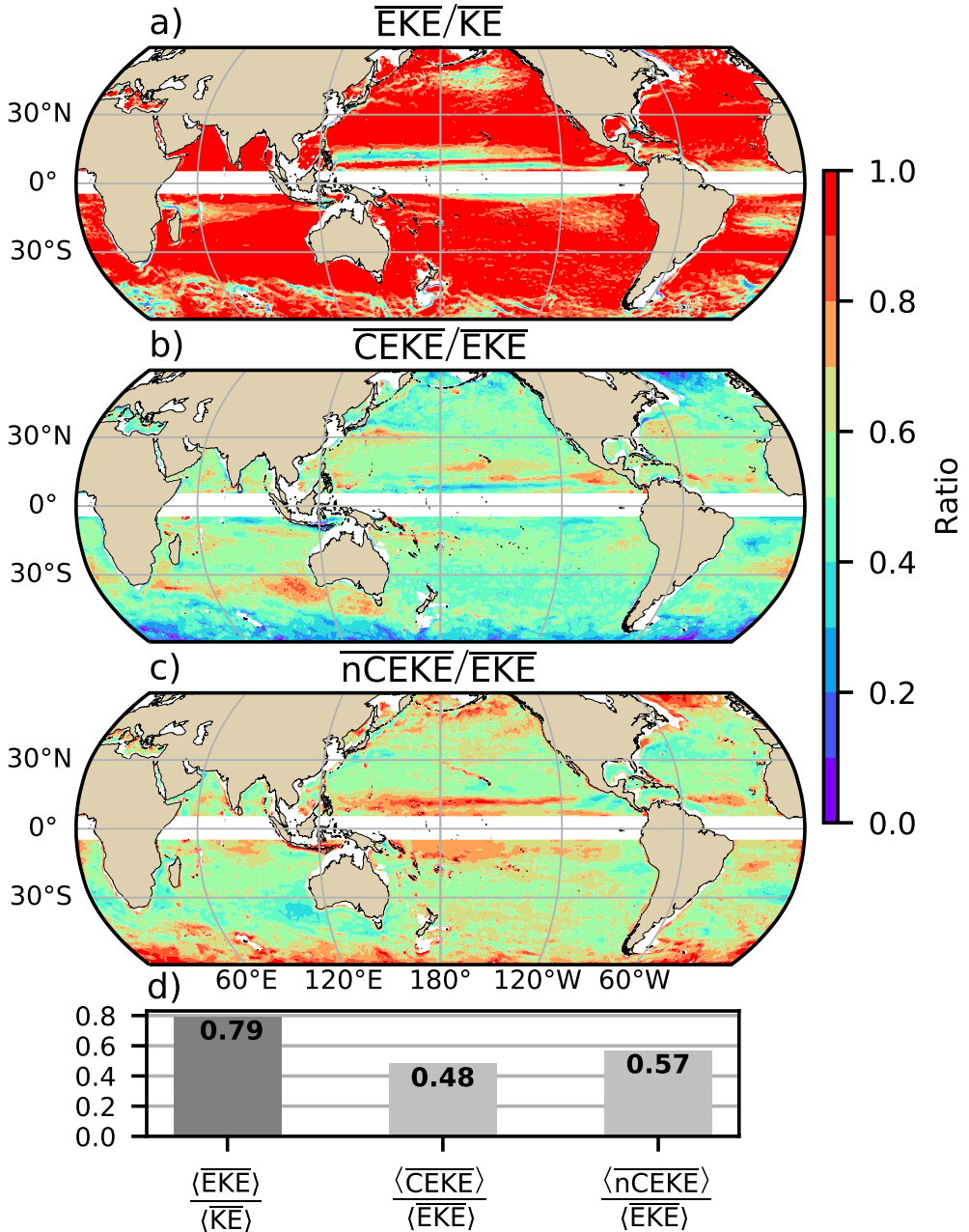
Eddy kinetic energy is known to be more than an order of magnitude greater than kinetic energy of the mean flow (MKE; Gill et al., 1974); this result is clearly shown in Figure 3a, which indicates that  $\overline{EKE}$  is responsible for almost all the  $\overline{KE}$  across the ocean, except for regions with persistent currents over time. Such regions are located in the mean boundary extension locations, the equatorial Pacific currents and regions in the Antarctic Circumpolar Current, where the  $\overline{EKE}$  explains around 40% of the  $\overline{KE}$ . In a previ-



200 **Figure 2.** a) Mean surface kinetic energy ( $\overline{KE}$ ); b) surface eddy kinetic energy ( $\overline{EKE}$ ); c)  
201 surface coherent eddy kinetic energy ( $\overline{CEKE}$ ), and d) surface non-coherent eddy kinetic energy  
202 ( $\overline{nCEKE}$ ) averaged between 1993-2018.

218 ous study, Chelton et al. (2011) estimated that the EKE within coherent eddies with life-  
219 times greater than 4 weeks contain between 40-60% of the  $\overline{EKE}$ . Our method to recon-  
220 struct the coherent eddy signature (Figure 3b) further corroborates that the coherent  
221 eddy component ( $\langle \overline{CEKE} \rangle$ ) has  $\sim 48\%$  of the  $\langle \overline{KE} \rangle$  (Figure 3d). Furthermore, global area  
222 averages of the ratios show that  $\langle \overline{EKE} \rangle$  explains  $\sim 78\%$  of the ocean  $\langle \overline{KE} \rangle$  field, while  
223 non coherent eddy features contain  $\sim 57\%$  percent of the  $\langle \overline{EKE} \rangle$ . Note that the globally  
224 averaged coherent and non coherent components do not add to 100% as the cross terms  
225 ( $O_c^2$ ) are non-zero. The spatial pattern reveals a dominance of the  $\overline{CEKE}$  equatorward  
226 from the boundary current extensions and in areas with large coherent eddy contribu-  
227 tions of around 80% of the region's eddy kinetic energy, such as south of Australia, in  
228 the Tehuantepec Gulf, and in the tropical Atlantic. An evident signal is a reduction of  
229 the energy contained by coherent eddies at high latitudes and an increase in the energy  
230 explained by non-coherent eddies; this signal could be a consequence of the inability of  
231 the 0.25° satellite resolution ( $\sim 13$  km at 60° latitude) to resolve coherent eddies with  
232 scales smaller than  $\sim 10$  km (first baroclinic Rossby radius at 60°; Chelton et al., 1998).

233 Figure 4 shows the seasonal cycle of the area-weighted EKE and CEKE for the North-  
234 ern Hemisphere ( $\langle EKE \rangle_{NH}$  and  $\langle CEKE \rangle_{NH}$ ; 10°N - 60°N) and Southern Hemisphere  
235 ( $\langle EKE \rangle_{SH}$  and  $\langle CEKE \rangle_{SH}$ ; 60°S - 10°S). In both hemispheres, the  $\langle EKE \rangle$  and  $\langle CEKE \rangle$   
236 peak during summer. In the Northern Hemisphere, the largest  $\langle EKE \rangle_{NH}$  and  $\langle CEKE \rangle_{NH}$



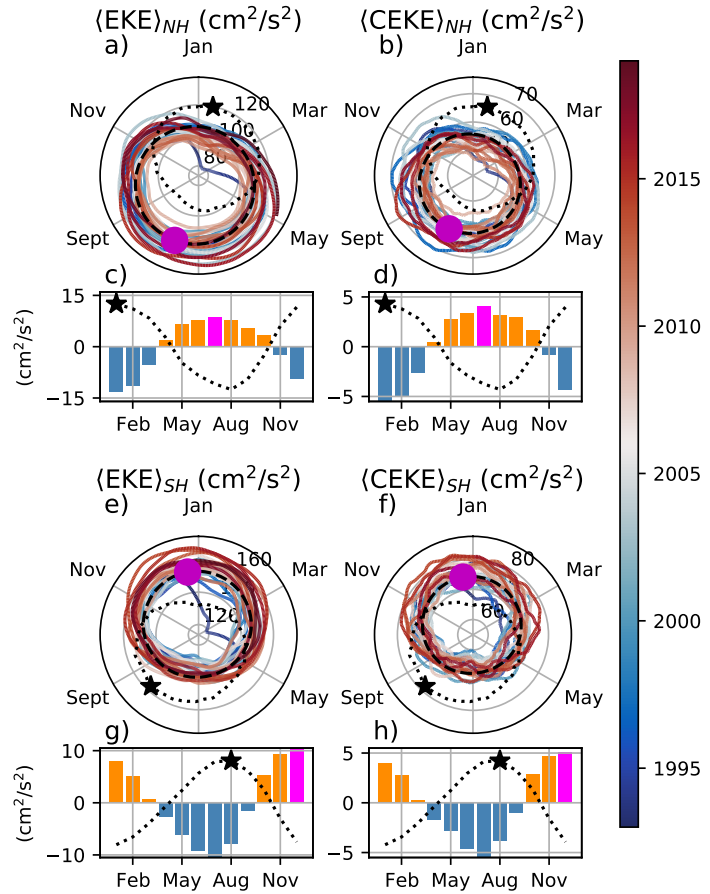
203 **Figure 3.** Ratios of the kinetic energy components. a) Map of the proportion of mean eddy  
 204 kinetic energy ( $\overline{\text{EKE}}$ ) versus mean kinetic energy ( $\overline{\text{KE}}$ ); b) Map of the fraction of mean coherent  
 205 eddy kinetic energy ( $\overline{\text{CEKE}}$ ) versus mean eddy kinetic energy ( $\overline{\text{EKE}}$ ); c) Map of the fraction of  
 206 mean non-coherent eddy kinetic energy ( $\overline{\text{nCEKE}}$ ) versus mean eddy kinetic energy ( $\overline{\text{EKE}}$ ); d)  
 207 Global time and area averaged (represented by  $\langle \rangle$ ) fraction of mean eddy kinetic energy ( $\langle \overline{\text{EKE}} \rangle$ )  
 208 versus the global mean kinetic energy ( $\langle \overline{\text{KE}} \rangle$ ), area averaged fraction of mean coherent eddy  
 209 kinetic energy ( $\langle \overline{\text{CEKE}} \rangle$ ) and mean non coherent eddy kinetic energy ( $\langle \overline{\text{nCEKE}} \rangle$ ) versus global  
 210 mean eddy kinetic energy ( $\langle \overline{\text{EKE}} \rangle$ ). Regions where the depth of the ocean is shallower than  
 211 1000m are removed from the ratio estimation.

237 occurs in July,  $\sim$ 6 months after the maximum winds in January (purple bar and black  
 238 star in Figure 4c and d). Meanwhile, the Southern Ocean  $\langle \text{EKE} \rangle_{SH}$  and  $\langle \text{CEKE} \rangle_{SH}$  sea-  
 239 sonal maxima arises during December,  $\sim$ 4 months after the maximum winds in August  
 240 (purple bar and back star in Figure 4g, and h). This lag between winds and the eddy  
 241 and coherent eddy energy components is further discussed in Section 4.

242 The cyclic plots in Figure 4 show the temporal evolution of  $\langle \text{EKE} \rangle$  and  $\langle \text{CEKE} \rangle$ .  
 243 Note that high frequency variability can be observed in the  $\langle \text{CEKE} \rangle$  field with tempo-  
 244 ral scales of a few months, this variability could be attributed to regional dynamics av-  
 245 eraged over the hemisphere (boundary currents, ocean gyres, etc.), as well as errors within  
 246 the coherent eddy reconstruction. Additionally, concentric changes in the cyclic plots high-  
 247 light long-term changes over the record. For example, the Northern Hemisphere winters  
 248 during early years of the record (blue) had a more energetic coherent eddy field, which  
 249 has transitioned to weaker coherent energy content since 2010 (red), in other words, the  
 250 intensity of the  $\langle \text{CEKE} \rangle_{NH}$  field has decreased. A larger long-term change can be ob-  
 251 served in the Southern Hemisphere, where concentric growth over time in  $\langle \text{EKE} \rangle_{SH}$  and  
 252  $\langle \text{CEKE} \rangle_{SH}$  supports the previously observed strengthening of the eddy field in the South-  
 253 ern Ocean (Hogg et al., 2015; Martínez-Moreno et al., 2019; Martínez-Moreno et al., 2021).

## 263 4 Global Coherent Eddy Statistics

264 Coherent eddy kinetic energy allows us to quantify and study the energy of the eddy  
 265 field, but the coherent eddy properties computed by automated coherent eddy identi-  
 266 fication algorithms allow us to further investigate the contribution and temporal changes  
 267 of their abundance (i.e. the number of eddies) and their intensity (both their amplitude  
 268 and diameter). Figure 5 shows gridded estimates of the number of eddies and the eddy  
 269 amplitude. In this analysis, we contrast our MM19 eddy count with that of CS13 (Chel-  
 270 ton et al., 2007; Figure 5a-b). Although the number of identified eddies is larger in MM19,  
 271 possibly due to the lifespan filter implemented by CS13, both datasets reveal consistent  
 272 spatial patterns. For example, both datasets show an important meridional variation in  
 273 the abundance of eddies, with high numbers of eddies in mid-latitudes and fewer eddies  
 274 in the tropics and at high-latitudes ( $\sim$ 60°). Additionally, there is a tendency at mid-latitudes  
 275 (30°) for higher numbers of eddies in the eastern side of ocean basins (e.g. the East North  
 276 Pacific, East North Atlantic, East South Pacific, and East South Atlantic). Another in-  
 277 teresting pattern emerges in both eddy count datasets, where small scale structures ap-



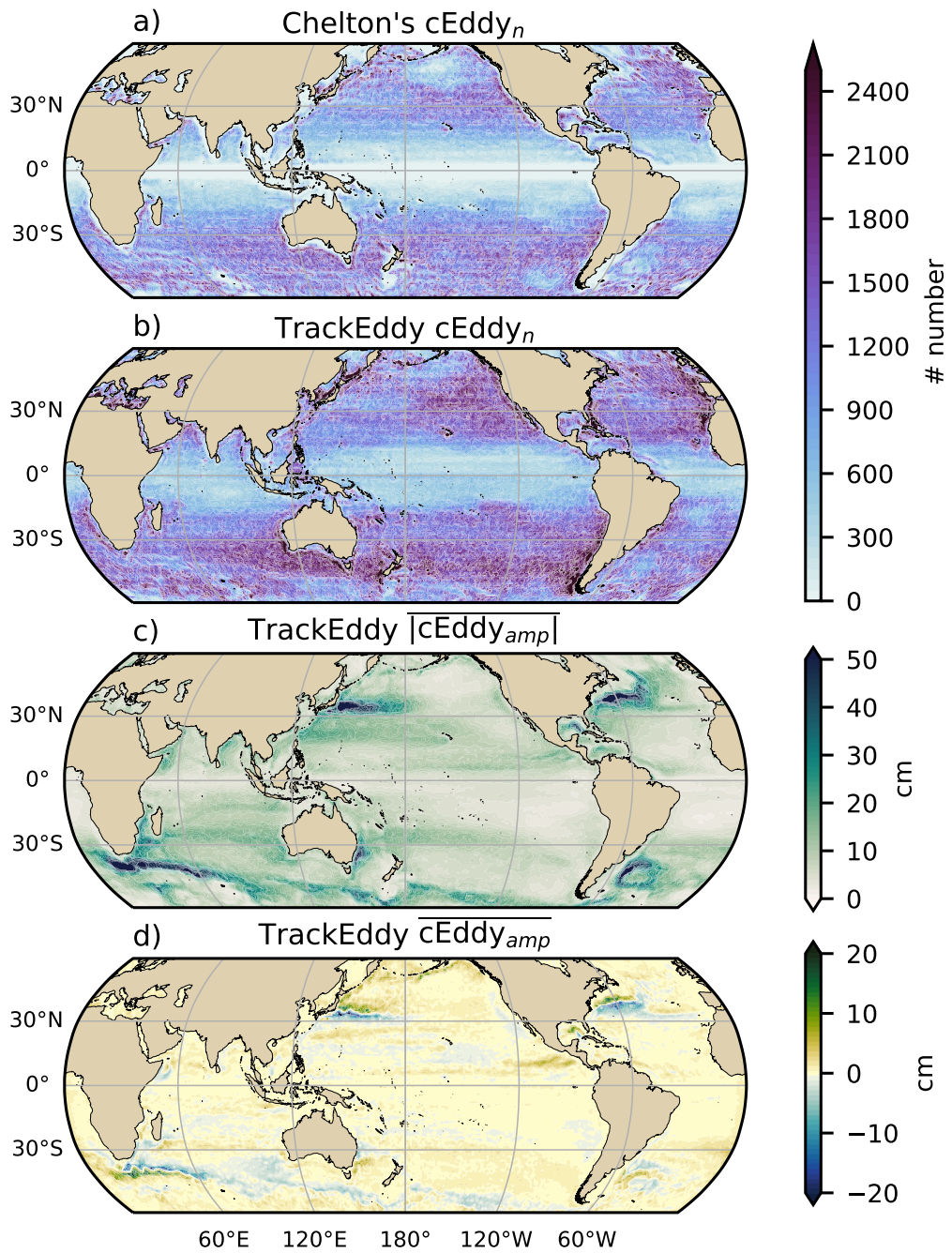
254 **Figure 4.** Seasonality of the area-weighted eddy kinetic energy ( $\langle EKE \rangle$ ) and coherent eddy  
 255 kinetic energy ( $\langle CEKE \rangle$ ). Panels a) and b) show the time-series of the Northern Hemisphere,  
 256 while panels e) and f) correspond to the Southern Hemisphere. Panels c) and d) show the sea-  
 257 sonal cycle of the  $\langle EKE \rangle_{NH}$  and  $\langle CEKE \rangle_{NH}$  in the Northern Hemisphere, and panels g) and h)  
 258 show the Southern Hemisphere ( $\langle EKE \rangle_{SH}$  and  $\langle CEKE \rangle_{SH}$ ). Dashed lines correspond to the sea-  
 259 sonal cycle of the fields and dotted lines show the seasonal cycle of the wind magnitude smoothed  
 260 over 120 days (moving average). The black stars and magenta markers (circle and bar) show  
 261 the maximum of the seasonal cycle for the kinetic energy components and the wind magnitude,  
 262 respectively. In the cyclic plots, line colors shows the year.

pear in the eddy count field. These small structures highlight preferred coherent eddy paths observable in boundary current extensions and over regions of the Southern Ocean. These structures and paths of coherent eddies could be associated with topographic features, with overall consistency between the eddy count patterns using the two different eddy identification methods.

Regions with large counts of eddies have, in general, small absolute amplitudes (Figure 5c), for example, the eastern side of mid-latitude ocean basins. The ocean gyre interiors have a larger absolute amplitude and finally regions such as the boundary current extensions and the Antarctic Circumpolar Current have the largest coherent eddy absolute amplitudes, as also shown by Chelton et al. (2011). Eddy amplitude highlights regions dominated by a given coherent eddy polarity, for example, boundary extensions have a preferred sign (Figure 5 d); namely, positive amplitude polewards of the boundary current extension mean location, and negative amplitude equatorwards. This sign preference is consistent with the preferential way that coherent eddies are shed from boundary current extensions; with warm core eddies (positive) polewards of the boundary current extension, and equatorward for cold core eddies (negative) (Chelton et al., 2007, 2011; Kang & Curchitser, 2013). These global statistics reveal the absolute coherent eddy amplitude as a proxy for the CEKE with similar spatial patterns (Figure 2 & Figure 5c) and showcases that in regions where  $\overline{\text{CEKE}}$  has a large proportion of  $\overline{\text{EKE}}$  (Figure 3), the absolute coherent eddy amplitude is also large.

To further understand the seasonal cycle of  $\langle \text{CEKE} \rangle$ , we compute the climatology of coherent eddy properties in each hemisphere (Figure 6). The seasonality of the number of eddies in the Northern Hemisphere peaks in April (Figure 6a, c), while the Southern Hemisphere maximum number of eddies occurs during October (Figure 6e, g). Meanwhile, the seasonality of the eddy amplitude ( $\langle |c\text{Eddy}_{amp}| \rangle$ ) peaks in August and January for the Northern and Southern Hemispheres respectively (Figure 6b, d, f, and h). As expected, the seasonality of  $\langle |c\text{Eddy}_{amp}| \rangle$ , equivalent to the intensity of the coherent eddies, is consistent with the seasonal cycle of  $\langle \text{CEKE} \rangle$ .

A key feature of Figure 6 is a distinct lag of  $\sim 3$  months between the winds and eddy count, while the eddy amplitude maximum occurs  $\sim 6$  months after the seasonal maxima in winds. We suggest that the eddy number increases earlier in the year and, through eddy-eddy interactions (merging of coherent eddies), the coherent eddy amplitude in-

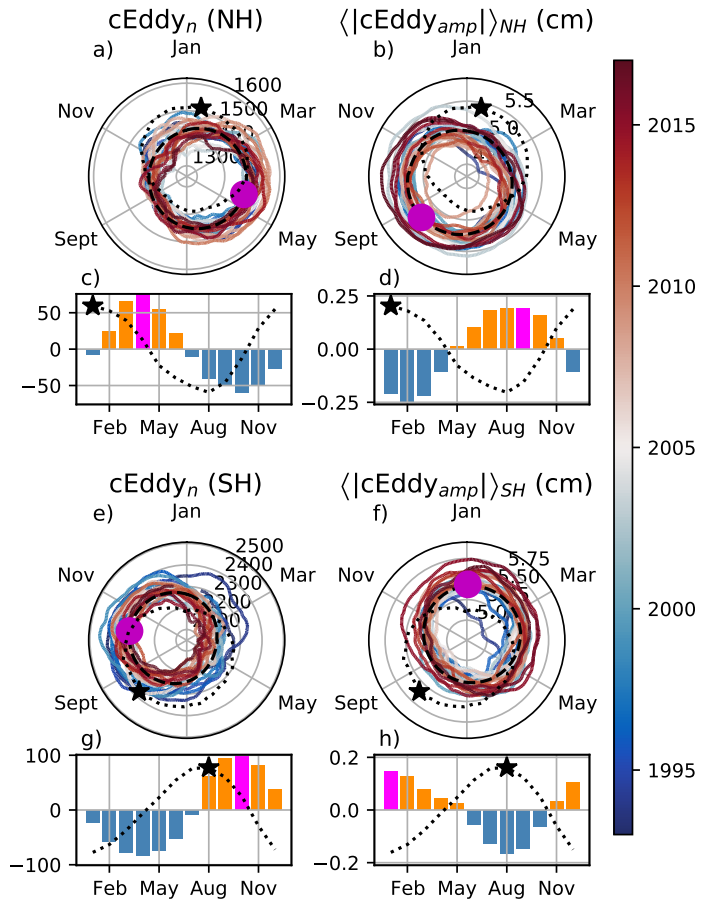


283 **Figure 5.** Averaged coherent eddy statistics. a) Climatology of the number of coherent eddies  
 284 (cEddy<sub>n</sub>) identified by Chelton et al. (2007); b) Climatology of the number of coherent eddies  
 285 (cEddy<sub>n</sub>) identified by Martínez-Moreno et al. (2019); c) Climatology of the mean absolute co-  
 286 herent eddy amplitude (cEddy<sub>amp</sub>), and d) Climatology of the mean coherent eddy amplitude  
 287 (cEddy<sub>amp</sub>).

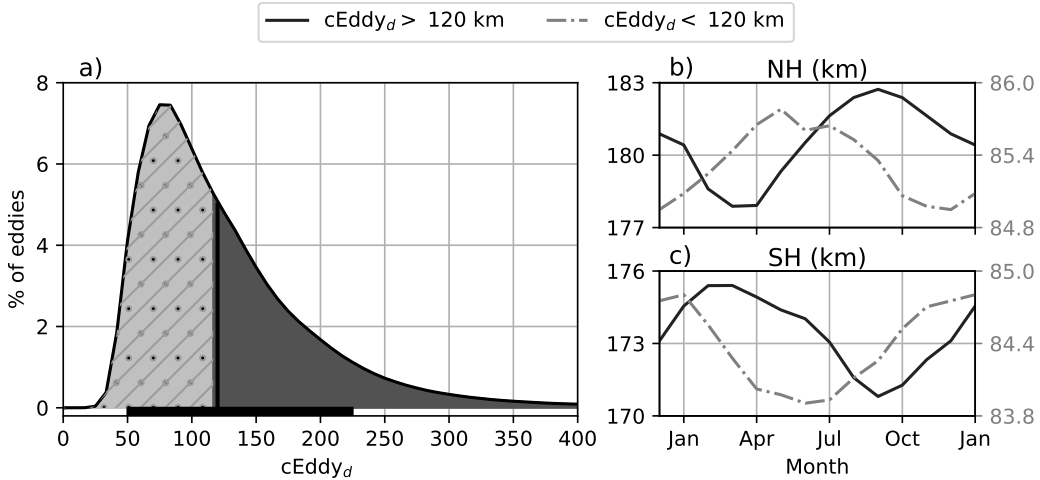
315 creases  $\sim$ 3 months after. This seasonal lag and summer maxima is consistent with pre-  
 316 vious studies which suggest that a time-lag of the inverse cascade (Sasaki et al., 2014;  
 317 Qiu et al., 2014) is responsible for the EKE seasonal cycle, where winter has the high-  
 318 est energy at the smallest scales (non-resolvable with satellite observations), spring and  
 319 autumn have the highest and lowest energy at scales of 50-100 km, and summertime has  
 320 the highest energy at the largest scales ( $> 100$  km; Uchida et al., 2017). Thus, the max-  
 321 imum of  $\langle \text{EKE} \rangle$ ,  $\langle \text{CEKE} \rangle$ , and  $\langle |c\text{Eddy}_{amp}| \rangle$  located during summertime suggests that  
 322 the seasonality of eddies and coherent eddies could be dominated by scales larger than  
 323 100 km.

324 This result can be further explored by looking at the seasonal evolution of the eddy  
 325 diameter ( $c\text{Eddy}_d$ ). Note that 90% of identified coherent eddies have diameters between  
 326 50 to 220 km (Figure 7a). We partition eddies into large-scale coherent eddies (diam-  
 327 eter  $> 120$  km) and small-scale coherent eddies (diameter  $< 120$  km; Figure 7a). In the  
 328 Northern Hemisphere, small-scale eddies have a seasonal peak in diameter during May,  
 329 while large-scale eddies have the greatest diameter in September (Figure 7b). Meanwhile,  
 330 in the Southern Hemisphere, the small-scale coherent eddies exhibit maximum dia-  
 331 meter in December, while the diameter of large-scale coherent eddies peaks in February (Fig-  
 332 ure 7 c). This result suggests that wind driven baroclinic instabilities generate small co-  
 333 herent eddies early in the season, which then merge and grow to become larger in diam-  
 334 eter and amplitude, and thus, more energetic. This process is likely associated with the  
 335 inverse energy cascade, and suggests that this mechanism not only drives EKE season-  
 336 ality, but also may be responsible for the seasonal cycle of coherent eddies.

352 Long-term changes can be observed in Figure 6a,b, e, and f where growing/shrinking  
 353 concentric circles over time denote an increase/decrease trend of the field. This trend  
 354 is particularly evident in the Southern Hemisphere, where the number of eddies has de-  
 355 creased, while the eddy amplitude has increased. This result is consistent with the ob-  
 356 served trends in EKE and mesoscale EKE in the Southern Ocean (Hogg et al., 2015; Martínez-  
 357 Moreno et al., 2019). The coherent eddy amplitude from positive coherent eddies and  
 358 negative coherent eddies show similar seasonal cycles to the absolute eddy amplitude.  
 359 The Northern Hemisphere decrease in absolute eddy amplitude is driven by a decrease  
 360 of the amplitude of negative coherent eddies in the Northern Hemisphere. Meanwhile  
 361 in the Southern Ocean, the increase in absolute eddy amplitude is corroborated by a strength-  
 362 ening of both coherent eddy polarities since the early 90s.



337 **Figure 6.** Seasonality of the count of number of eddies ( $c\text{Eddy}_n$ ) and the area-weighted polar-  
 338 erty independent coherent eddy amplitude ( $\langle |c\text{Eddy}_{amp}| \rangle$ ); Panels a and b show the time-series of  
 339 the Northern Hemisphere, while panels e and f correspond to the Southern Hemisphere. Panels  
 340 c and d show the seasonal cycle of  $c\text{Eddy}_n$  and  $\langle |c\text{Eddy}|_{amp} \rangle_{NH}$  in the Northern Hemisphere,  
 341 and panels g and h show the Southern Hemisphere,  $c\text{Eddy}_n$  and  $\langle |c\text{Eddy}|_{amp} \rangle_{SH}$ . Dashed lines  
 342 correspond to the seasonal cycle of the fields and dotted lines show the seasonal cycle of the wind  
 343 magnitude, smoothed over 120 days (moving average). The black stars and magenta markers  
 344 (circle and bar) indicate the maximum of the seasonal cycle for the eddy property, and the wind  
 345 magnitude, respectively. In the cyclic plots, line colors show the year from 1993-2019.

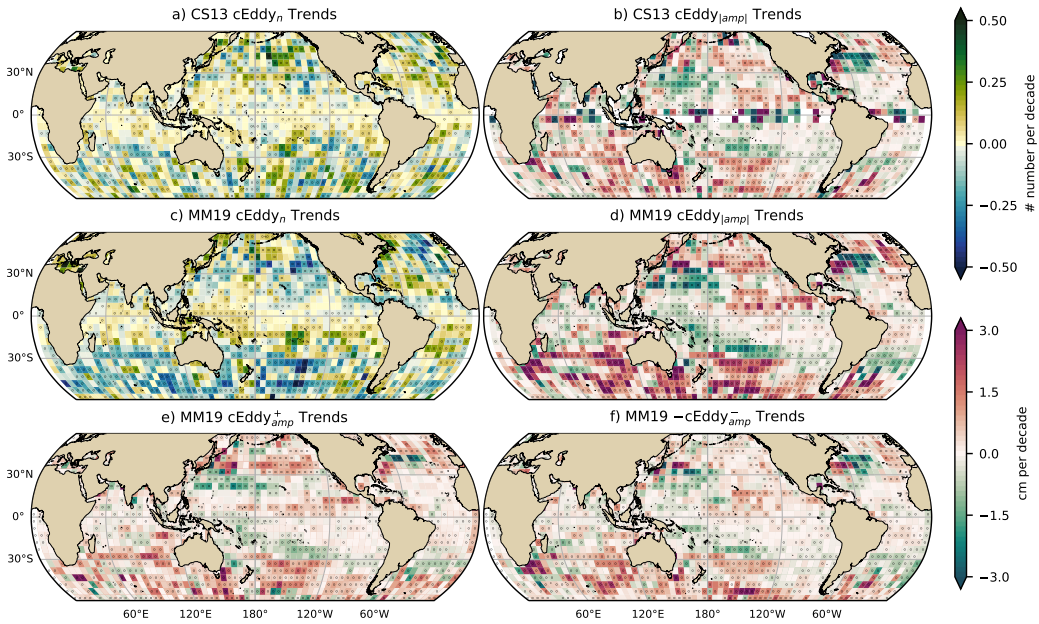


346 **Figure 7.** Distribution of the identified eddy diameter ( $cEddy_d$ ; km) and hemispherical  
 347 seasonality of the coherent eddy diameter. a) Distribution in percentage of identified eddy am-  
 348 plitude, solid bar below distribution represents 90% of the identified eddies. Seasonal cycle of  
 349 the eddy diameter for the b) Northern Hemisphere and c) Southern Hemisphere. Dark solid line  
 350 and area corresponds to coherent eddies with diameters larger than 120 km, while light gray  
 351 dash-dotted line and area shows coherent eddies with diameters smaller than 120 km.

## 363 5 Trends

364 The results presented in Figures 4 and 6 suggest a long-term readjustment of the  
 365 coherent eddy field. The long-term trends of the number of coherent eddies, absolute co-  
 366 herent eddy amplitude, and coherent eddy amplitude polarities are further explored in  
 367 Figure 8 contrasting the MM19 and CS13 methods. Both MM19 and CS13 datasets show  
 368 consistent spatial patterns in the trends and significance of the number of coherent ed-  
 369 dies and the absolute coherent eddy amplitude. Several regions in the ocean, such as the  
 370 Southern Ocean, North Atlantic and North Pacific, show a decrease in the number of ed-  
 371 dies. Those same regions also have a clear increase in the absolute coherent eddy am-  
 372 plitude. These trends are similar to those observed in mesoscale eddy kinetic energy (Martínez-  
 373 Moreno et al., 2021) and provide additional evidence of a readjustment of the mesoscale  
 374 eddy field over the last 3 decades.

375 The observed trends of  $cEddy_{amp}$  in several oceanic regions have the same scale  
 376 as sea level rise ( $\sim 3$  cm per decade). By analyzing the positive and negative coherent eddy  
 377 amplitude, we filter out the observed trends that come from a net increase in sea level.



385 **Figure 8.** Trends of coherent eddy statistics. a) and b) Trends of the number of identified  
 386 coherent eddies from satellite observations identified using the TrackEddy scheme of MM19,  
 387 and those reported in CS13’s dataset. c) and d) Trends of the absolute value of identified coher-  
 388 ent eddy amplitude ( $cEddy_{amp}$ ) from satellite observations identified using TrackEddy (after  
 389 MM19), and those reported by CS13. e) and f) Trends of the eddy amplitude polarity using  
 390 TrackEddy ( $cEddy_{amp}^+$  and  $cEddy_{amp}^-$ ). Gray stippling shows regions that are statistically signifi-  
 391 cant above the 95% confidence level.

378 In fact, each coherent eddy polarity has intensified in the Southern Ocean and North East  
 379 Pacific and Atlantic. In other words, the amplitude of each polarity has increased over  
 380 time, and thus this strengthening is an intrinsic response of the coherent eddy field. Note  
 381 that the negative coherent eddy amplitude dominates the global  $|cEddy_{amp}|$  trends (Fig-  
 382 ure 8e, f). However, different trend patterns can be observed in both positive and neg-  
 383 ative coherent eddy amplitudes in the North Atlantic and North Pacific, where the neg-  
 384 ative coherent eddy amplitude in the Western Boundary Currents appears to decrease.

## 392 6 Regional Climatology

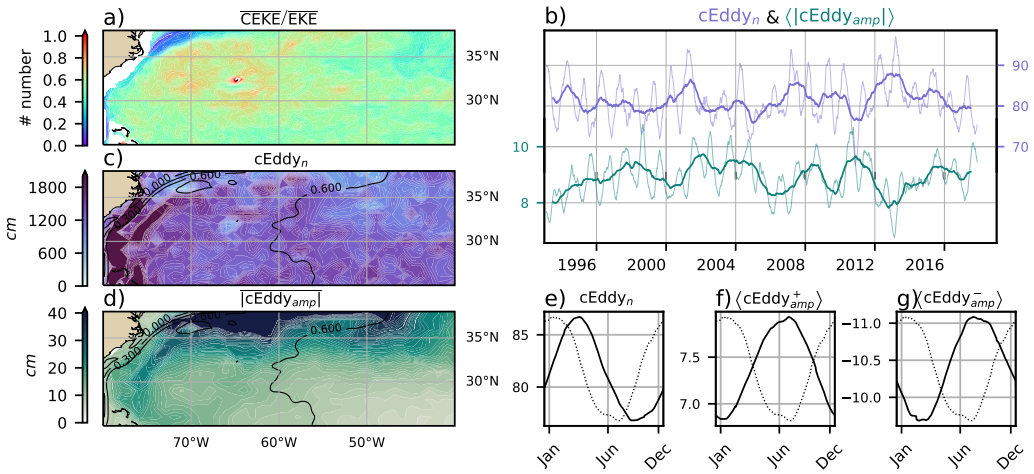
393 For regions with relatively large proportions of CEKE located at WBC extensions  
 394 and eastern boundary currents, we investigate the seasonal and long-term variability of  
 395 the coherent eddy properties. The most energetic WBC include the Gulf Stream, the Kuroshio

396 Current, and the Agulhas Current (Figures 9, 10, and 11). Coherent eddy generation in  
 397 boundary current extensions occurs through baroclinic and barotropic instabilities of the  
 398 mean current, thus all these regions share similar generation dynamics. In all these re-  
 399 gions without exception; (i) CEKE contains 50-80% of the EKE in regions equatorward  
 400 from the mean WBC extensions, (ii) the number of eddies is consistently small over the  
 401 mean WBC extensions, and (iii) the eddy amplitude is larger over the mean WBC ex-  
 402 tensions.

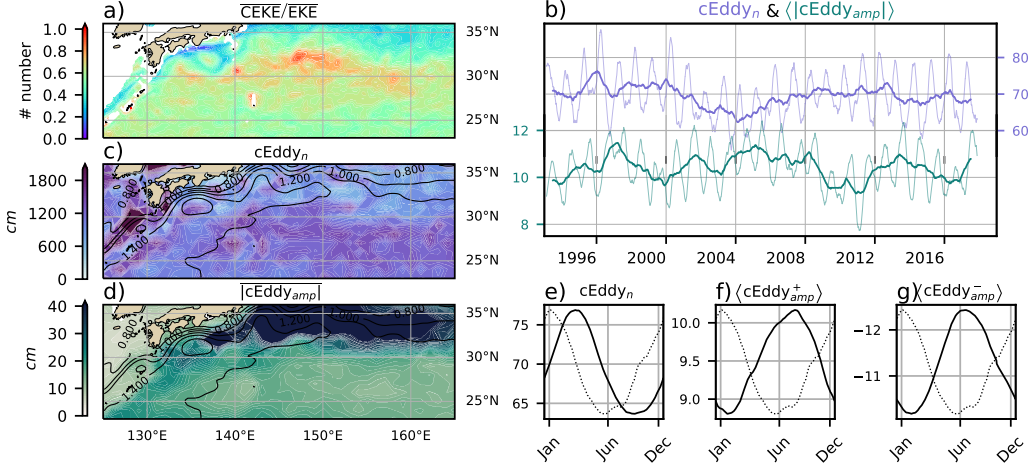
403 In the Gulf Stream, the energy ratio between CEKE and EKE is  $\sim$ 56% (Figure 9).  
 404 The highest energy ratio occurs in regions with numerous eddies, colocated with regions  
 405 where the largest  $|cEddy_{amp}|$  gradients occur. The time series of  $cEddy_n$  and  $\langle |cEddy_{amp}| \rangle$   
 406 are anti-correlated (-0.52), and they display interannual and seasonal variability. Although  
 407 Chaudhuri et al. (2009) observed that a positive phase of the North Atlantic Oscillation  
 408 (NAO) exhibits higher EKE, due to an increase in baroclinic instability, thus suggest-  
 409 ing more coherent eddies, we do not find a correlation between the  $cEddy_n$  or the  $\langle |cEddy_{amp}| \rangle$   
 410 in the Gulf Stream and the NAO index. Similar to the signal observed in the hemispheric  
 411 analysis, the eddy count seasonal cycle follows the wind maximum lagging by  $\sim$ 3 months,  
 412 while the amplitude of the coherent eddies lags by  $\sim$  6 months.

421 The variability of the  $cEddy_n$  and  $\langle |cEddy_{amp}| \rangle$  in the Kuroshio Current are weakly  
 422 anti-correlated (-0.41; Figure 10). However, on average 56% of the energy in the region  
 423 corresponds to CEKE. As observed in the Gulf Stream, there is an important seasonal  
 424 cycle in the boundary extension, where the eddy count seasonal cycle occurs in March,  
 425 lagging the wind maximum by  $\sim$ 3 months (January). Meanwhile, the amplitude of the  
 426 coherent eddies lags the wind maximum by  $\sim$  6 months (June).

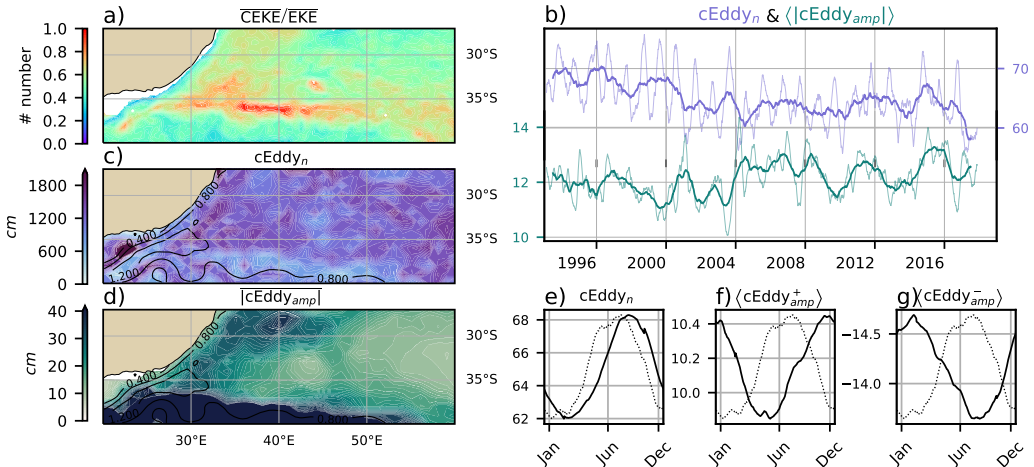
433 In the Southern Hemisphere the strongest boundary current, the Agulhas Current,  
 434 shows similar behavior to its counterparts in the Northern Hemisphere (Figure 11). On  
 435 average, coherent eddies in the Agulhas Current contain  $\sim$ 56% of the energy, meanwhile  
 436 the  $cEddy_n$  seasonal peak occurs in August, while the  $\langle |cEddy_{amp}| \rangle$  peak occurs in January-  
 437 February. The seasonal lag between the winds, eddy count, and eddy amplitude in each  
 438 of the WBC extensions is interpreted as being analogous to the lagged response of co-  
 439 herent eddy properties (Figure 6) due to eddy-eddy interactions, consistent with the in-  
 440 verse cascade of energy.



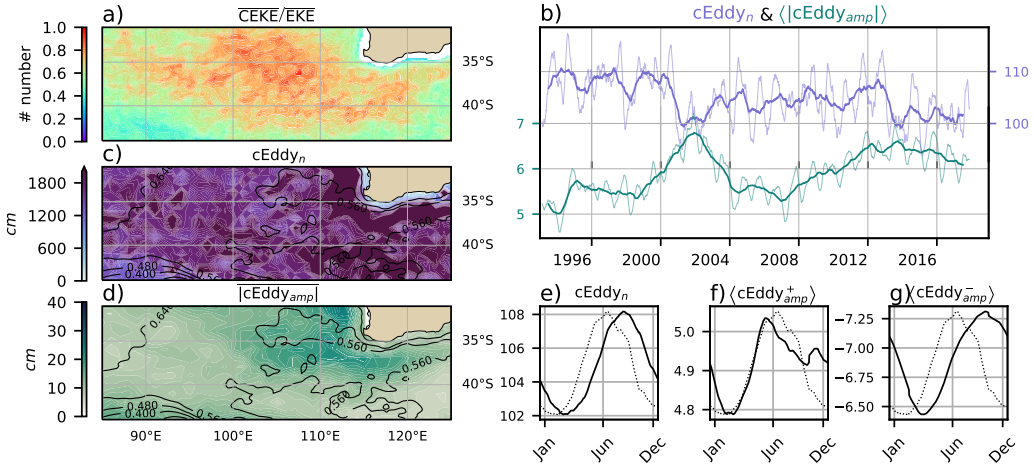
413 **Figure 9.** Climatology of the eddy field and coherent eddy field in the Gulf Stream. a) Ratio  
 414 of mean coherent eddy kinetic energy ( $\overline{CEKE}$ ) versus mean eddy kinetic energy ( $\overline{EKE}$ ); b) Thick  
 415 lines show the running average over 2 years and thin lines show the running average over 90 days  
 416 of the coherent eddy number sum and the average coherent eddy amplitude; c) Map of the num-  
 417 ber of eddies; d) Map of the average coherent eddy amplitude; e) Seasonal cycle of the number  
 418 of eddies ( $cEddy_n$ ); f) Seasonal cycle of the positive coherent eddy amplitude ( $\langle cEddy_{amp}^+ \rangle$ ),  
 419 and g) Seasonal cycle of the negative coherent eddy amplitude ( $\langle cEddy_{amp}^- \rangle$ ). Contours in maps  
 420 correspond to mean sea surface height (m).



427 **Figure 10.** As in Figure 9, only showing the climatology of the eddy field and coherent eddy  
 428 field in the Kuroshio extension. a) Ratio of mean coherent eddy kinetic energy ( $\overline{\text{CEKE}}$ ) versus  
 429 mean eddy kinetic energy ( $\overline{\text{EKE}}$ ); b) Time-series of the coherent eddy number and the average  
 430 coherent eddy amplitude; c) Map of the number of eddies; d) Map of the average coherent eddy  
 431 amplitude; Seasonal cycle of the e) number of eddies; f) positive coherent eddy amplitude, and g)  
 432 negative coherent eddy amplitude.



441 **Figure 11.** As in Figure 9, only showing the climatology of the eddy field and coherent eddy  
 442 field in the Agulhas Current. a) Ratio of mean coherent eddy kinetic energy ( $\overline{\text{CEKE}}$ ) versus  
 443 mean eddy kinetic energy ( $\overline{\text{EKE}}$ ); b) Time-series of the coherent eddy number and the average  
 444 coherent eddy amplitude; c) Map of the number of eddies; d) Map of the average coherent eddy  
 445 amplitude; Seasonal cycle of the e) number of eddies; f) positive coherent eddy amplitude, and g)  
 446 negative coherent eddy amplitude.



457 **Figure 12.** As in Figure 9, only showing the climatology of the eddy field and coherent eddy  
 458 field in the Leeuwin Current. a) Ratio of mean coherent eddy kinetic energy ( $\overline{\text{CEKE}}$ ) versus  
 459 mean eddy kinetic energy ( $\overline{\text{EKE}}$ ); b) Time-series of the coherent eddy number and the average  
 460 coherent eddy amplitude; c) Map of the number of eddies; d) Map of the average coherent eddy  
 461 amplitude; Seasonal cycle of the e) number of eddies; f) positive coherent eddy amplitude, and g)  
 462 negative coherent eddy amplitude.

447 Coherent eddies dominate the EKE field in other regions such as the Leeuwin Cur-  
 448 rent (Figure 12), where 65% of the energy is contained by coherent eddies. The Leeuwin  
 449 region is not characterized by having a large EKE, however, a considerable abundance  
 450 of eddies and large eddy amplitudes are observed in the region. The time-series reveal  
 451 a significant increase in the  $\langle |c\text{Eddy}_{amp}| \rangle$ , while the  $c\text{Eddy}_n$  has decreased over the last  
 452 3 decades. The seasonal cycle shows that the  $c\text{Eddy}_n$  peak occurs in August, 3 months  
 453 after the maximum winds (June). Meanwhile, the  $\langle c\text{Eddy}_{amp}^+ \rangle$  responds in synchrony  
 454 to the winds, and the  $\langle c\text{Eddy}_{amp}^- \rangle$  is in phase with the seasonal cycle of the eddy num-  
 455 ber ( $c\text{Eddy}_n$ ). Hence, this region contrasts the behavior of WBC extensions, and show-  
 456 cases the spatial variability of the seasonal cycle of coherent eddies.

463 Another region with important contributions to the coherent eddy field is the East  
 464 Tropical Pacific (Tehuantepec region; Figure 13), where coherent eddies contain  $\sim 58\%$   
 465 of the energy. In fact, coherent eddy generation in this region is modulated by winds and  
 466 coastally trapped waves which produce a strong horizontal and vertical shear (baroclinic  
 467 and barotropic instabilities; Zamudio et al., 2006). Furthermore, the equatorial gener-

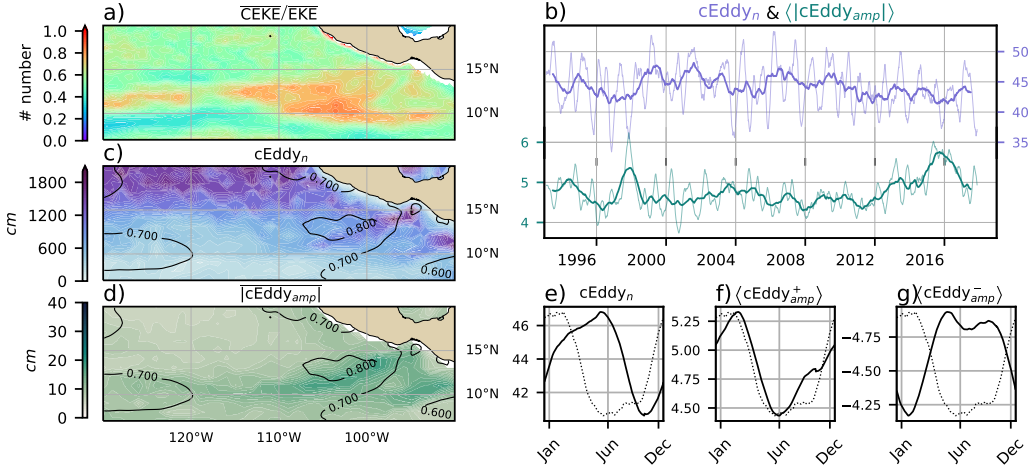


**Figure 13.** As in Figure 9, only showing the climatology of the eddy field and coherent eddy field in the East Tropical Pacific. a) Ratio of mean coherent eddy kinetic energy ( $\overline{\text{CEKE}}$ ) versus mean eddy kinetic energy ( $\overline{\text{EKE}}$ ); b) Time-series of the coherent eddy number and the average coherent eddy amplitude; c) Map of the number of eddies; d) Map of the average coherent eddy amplitude; Seasonal cycle of the e) number of eddies; f) positive coherent eddy amplitude, and g) negative coherent eddy amplitude.

ated waves propagating along the coast have an important interannual variability observable in the  $\langle |c\text{Eddy}_{amp}| \rangle$  time-series, where El Niño events are notable during 1997 and 2015 (Figure 13b). The seasonal cycle of  $c\text{Eddy}_n$ ,  $\langle c\text{Eddy}_{amp}^+ \rangle$ , and  $\langle c\text{Eddy}_{amp}^- \rangle$  support the idea of a coherent eddy response to two different coherent eddy generation mechanisms; the number of eddies lags by  $\sim 3$  months from the winds, while the  $\langle c\text{Eddy}_{amp}^+ \rangle$  is in phase with the winds and the time of maximum trapped wave activity (winter; Zamudio et al., 2006), while the  $\langle c\text{Eddy}_{amp}^- \rangle$  could be a consequence of eddy-eddy interactions.

## 7 Discussion and Conclusions

We have investigated the contribution of coherent eddies to the total kinetic energy field using available satellite observations. We found that around half of the EKE is explained by coherent eddies. This half is concentrated in eddy-rich regions where a recent multi-decadal intensification of the eddy field has been observed (Martínez-Moreno et al., 2021). The energy contained by eddies is larger than the previous estimate of 40%

488 by Chelton et al. (2011). Although there are differences in the identification criteria of  
489 both eddy identification methods, the main cause of the difference is likely to be the life-  
490 span and amplitude filters. These filters are widely used to track individual eddies in space  
491 and time, however, interactions between eddies in energetic regions may obscure the abun-  
492 dance and influence of short-lived coherent eddies. Filters are not used in this study, and  
493 indeed a lack of filters could facilitate an over-estimation of the energy contained by  
494 coherent eddies, when mis-identifying or mis-fitting a coherent eddy.

495 It should also be noted that regions with first baroclinic Rossby radius of defor-  
496 mation smaller than 10km cannot be resolved by satellite observations. Thus, the en-  
497 ergy contained by coherent eddies around latitudes of 60° and those near the shore are  
498 missed from this estimate, and their role in the seasonal cycle and local dynamics remains  
499 unknown . New satellite altimeter missions (e.g. Surface Water and Ocean Topography;  
500 SWOT) may allow estimates of the energy contained by mesoscale coherent eddies out-  
501 side the subtropical regions and over the continental slope.

502 Hemisphere-wide variability indicates a strong seasonal cycle of the EKE, CEKE,  
503 and eddy properties. The seasonal cycle of the CEKE in each hemisphere occurs as a  
504 consequence of numerous small coherent eddies interacting with each other (eddy-eddy  
505 interactions) and resulting in stronger, larger and more energetic (but fewer) coherent  
506 eddies during summer, after a few months of the yearly coherent eddy number maxima.  
507 This result reveals eddy-eddy interactions and thus the transfer of energy from smaller  
508 coherent eddies to larger coherent eddies could explain the observed seasonal cycle of CEKE  
509 and coherent eddies properties.

510 Coherent eddy properties reveal a non-uniform long-term readjustment of the mesoscale  
511 eddy field. Overall, the eddy number has decreased globally at a significant rate of  $\sim$ 35  
512 eddies per decade from  $\sim$ 4000 eddies identified globally on average each day. Despite the  
513 small changes in the total eddy numbers, large proportions of the ocean show a major  
514 strengthening of the mesoscale coherent eddy amplitude at rates greater than  $\sim$ 1 cm per  
515 decade. This strengthening of the coherent eddy amplitude is attributed to an intensi-  
516 fication of each coherent eddy polarity, rather than a readjustment of the coherent eddy  
517 field to sea level rise. In other words, the coherent eddy amplitude intensification is oc-  
518 ccurring in both coherent eddy polarities and explains a proportion of the previously ob-  
519 served readjustments in the eddy field to long-term changes in the ocean forcing (Hu et

520 al., 2020; Wunsch, 2020; Martínez-Moreno et al., 2021). This long-term readjustment re-  
521 veals an intensification of the coherent eddy field, possibly due to long-term readjust-  
522 ments in the ocean baroclinic and barotropic instabilities, as well as the strength of the  
523 winds.

524 The reconstruction of the coherent eddies and their statistics has revealed regions  
525 with important coherent eddy contributions and a distinct seasonal evolution of the co-  
526 herent eddies. Western boundary current (WBC) extensions generate eddies through the  
527 instability of the main currents and the seasonal cycle of coherent eddies, CEKE, and  
528 thus EKE could be associated with an inverse energy cascade observable through lagged  
529 seasonal cycles in the coherent eddy statistics. In addition, the amplitude of the seasonal  
530 cycle in WBC extensions is two times larger than any other region, thus the seasonal-  
531 ity of the coherent eddies in WBC extensions dominates the hemispheric seasonal cy-  
532 cle. Furthermore, the seasonal lag of the inverse energy cascade is coupled with the pres-  
533 ence of fronts (Qiu et al., 2014), such as the case for WBC extensions, and our results  
534 are consistent with the notion of baroclinic instability generating eddies and, via eddy-  
535 eddy interactions, a lagged inverse energy cascade.

536 The use of satellite observations in this study limits our ability to quantify the im-  
537 portance of the inverse energy cascade seasonality in the control of the coherent eddy  
538 seasonal cycle. As mentioned above, there is robust evidence of an increase in eddy-eddy  
539 interactions, however we cannot discard important contributions from other processes  
540 such as the seasonal cycle of forcing, stratification, and instabilities, which are crucial  
541 in the generation of coherent eddies. Although this study can provide a descriptive re-  
542 sponse of the coherent eddy field, further work is needed to assess the role of eddy-eddy  
543 interactions in our changing climate, ocean dynamics, and biogeochemical processes. Fur-  
544 thermore, the SWOT mission could allow us to advance our understanding of eddy-eddy  
545 interactions and the seasonal cycle of scales smaller than mesoscale, which may provide  
546 further evidence of the inverse energy cascade driving the coherent eddy seasonality. Cur-  
547 rent generation climate models have just started to resolve mesoscale dynamics, thus,  
548 the presented estimate of energy in coherent eddies from satellite observations could be  
549 used as a benchmark that facilitates the evaluation of such models, and to quantify the  
550 energy contained by mesoscale and more specifically coherent eddies in future climate  
551 projections.

552 **Acknowledgments**

The Chelton & Schlax (2013) dataset was produced by SSALTO/DUACS and distributed by AVISO+ (<https://www.aviso.altimetry.fr/>) with support from CNES, developed and validated in collaboration with E.Mason at IMEDEA. Global coherent eddy reconstruction, coherent and non-coherent eddy kinetic energy datasets, in addition to gridded coherent eddy tracking datasets are publicly available at (<https://doi.org/10.5281/zenodo.4646429>). All analyses and figures in this manuscript are reproducible via Jupyter notebooks and instructions can be found in the Github repository `CEKE_climatology` ([https://github.com/josuemtzmo/CEKE\\_climatology](https://github.com/josuemtzmo/CEKE_climatology)). Trends used the Python Package `xarrayMannKendall` (<https://doi.org/10.5281/zenodo.4458776>). J.M.-M. was supported by the Consejo Nacional de Ciencia y Tecnología (CONACYT), Mexico funding. M.H.E. is supported by the Centre for Southern Hemisphere Oceans Research (CSHOR), a joint research centre between Qingdao National Laboratory for Marine Science and Technology (QNLM), Commonwealth Scientific and Industrial Research Organisation (CSIRO), University of New South Wales (UNSW), and the University of Tasmania (UTAS). Analyses were undertaken on the National Computational Infrastructure in Canberra, Australia, which is supported by the Australian Commonwealth Government.

569 **References**

- 570 Arbic, B. K., Polzin, K. L., Scott, R. B., Richman, J. G., & Shriver, J. F. (2013).  
 571 On Eddy Viscosity, Energy Cascades, and the Horizontal Resolution of Gridded  
 572 Satellite Altimeter Products\*. *Journal of Physical Oceanography*, 43(2), 283–300.  
 573 doi: 10.1175/jpo-d-11-0240.1
- 574 Ashkezari, M. D., Hill, C. N., Follett, C. N., Forget, G., & Follows, M. J. (2016).  
 575 Oceanic eddy detection and lifetime forecast using machine learning methods.  
 576 *Geophysical Research Letters*, 43(23). doi: 10.1002/2016gl071269
- 577 Beron-Vera, F. J., Wang, Y., Olascoaga, M. J., Goni, G. J., & Haller, G. (2013). Ob-  
 578 jective Detection of Oceanic Eddies and the Agulhas Leakage. *Journal of Physical  
 579 Oceanography*, 43(7), 1426–1438. doi: 10.1175/JPO-D-12-0171.1
- 580 Bouali, M., Sato, O. T., & Polito, P. S. (2017). Temporal trends in sea surface tem-  
 581 perature gradients in the South Atlantic Ocean. *Remote Sensing of Environment*,  
 582 194, 100–114. doi: 10.1016/j.rse.2017.03.008
- 583 Callies, J., Flierl, G., Ferrari, R., & Fox-Kemper, B. (2015). The role of mixed-layer

- 584 instabilities in submesoscale turbulence. *Journal of Fluid Mechanics*, 788, 5–41.  
 585 doi: 10.1017/jfm.2015.700
- 586 Cane, M. A., Clement, A. C., Kaplan, A., Kushnir, Y., Pozdnyakov, D., Seager, R.,  
 587 ... Murtugudde, R. (1997). Twentieth-Century Sea Surface Temperature Trends.  
 588 *Science*, 275(5302), 957–960. doi: 10.1126/science.275.5302.957
- 589 Chaudhuri, A. H., Gangopadhyay, A., & Bisagni, J. J. (2009). Interannual variabil-  
 590 ity of Gulf Stream warm-core rings in response to the North Atlantic Oscillation.  
 591 *Continental Shelf Research*, 29(7), 856–869. doi: 10.1016/j.csr.2009.01.008
- 592 Chelton, D. B., A. d. R., Schlax, M. G., Naggar, K., & Siwertz, N. (1998). Geo-  
 593 graphical variability of the first baroclinic Rossby radius of deformation. *Journal*  
 594 *of Physical Oceanography*, 28(3), 433-460. doi: 10.1175/1520-0485(1998)028<433:  
 595 GVOTFB>2.0.CO;2
- 596 Chelton, D. B., Gaube, P., Schlax, M. G., Early, J. J., & Samelson, R. M. (2011).  
 597 The influence of nonlinear mesoscale eddies on near-surface oceanic chlorophyll.  
 598 *Science*, 334(6054), 328-32. doi: 10.1126/science.1208897
- 599 Chelton, D. B., & Schlax, M. G. (2013). *Mesoscale eddies in altimeter observations*  
 600 *of ssh*.
- 601 Chelton, D. B., Schlax, M. G., Samelson, R. M., & de Szoeke, R. A. (2007). Global  
 602 observations of large oceanic eddies. *Geophysical Research Letters*, 34(15),  
 603 L15606. doi: 10.1029/2007GL030812
- 604 CMEMS. (2017). The Ssalto/Duacs altimeter products were produced and dis-  
 605 tributed by the Copernicus Marine and Environment Monitoring Service. *Aviso*  
 606 *Dataset*. Retrieved from <https://www.aviso.altimetry.fr/>
- 607 Cui, W., Wang, W., Zhang, J., & Yang, J. (2020). Identification and census statis-  
 608 tics of multicore eddies based on sea surface height data in global oceans. *Acta*  
 609 *Oceanologica Sinica*, 39(1), 41–51. doi: 10.1007/s13131-019-1519-y
- 610 Faghmous, J. H., Frenger, I., Yao, Y., Warmka, R., Lindell, A., & Kumar, V. (2015,  
 611 6). A daily global mesoscale ocean eddy dataset from satellite altimetry. *Scientific*  
 612 *Data*, 2, 150028 EP -. doi: 10.1038/sdata.2015.28
- 613 Ferrari, R., & Wunsch, C. (2009). Ocean Circulation Kinetic Energy: Reservoirs,  
 614 Sources, and Sinks. *Annual Review of Fluid Mechanics*, 41(1), 253–282. doi: 10  
 615 .1146/annurev.fluid.40.111406.102139
- 616 Frenger, I., Gruber, N., Knutti, R., & Münnich, M. (2013). Imprint of Southern

- 617 Ocean eddies on winds, clouds and rainfall. *Nature Geoscience*, 6(8), 608 EP -.  
618 doi: 10.1038/ngeo1863
- 619 Frenger, I., Münnich, M., Gruber, N., & Knutti, R. (2015). Southern Ocean eddy  
620 phenomenology. *Journal of Geophysical Research: Oceans*, 120(11), 7413-7449.  
621 doi: 10.1002/2015JC011047
- 622 Fu, L., Chelton, D., Le Traon, P., & Oceanography, M. R. (2010). Eddy dynamics  
623 from satellite altimetry. *Oceanography*, 23(4), 14-25. doi: 10.2307/24860859
- 624 Gill, A., Green, J., & Simmons, A. (1974). Energy partition in the large-scale ocean  
625 circulation and the production of mid-ocean eddies. *Deep Sea Res Oceanogr Abstr*,  
626 21(7), 499-528. doi: 10.1016/0011-7471(74)90010-2
- 627 Hogg, A. M., & Blundell, J. R. (2006). Interdecadal variability of the southern  
628 ocean. *Journal of Physical Oceanography*, 36(8), 1626-1645. doi: 10.1175/  
629 JPO2934.1
- 630 Hogg, A. M., Meredith, M. P., Chambers, D. P., Abrahamsen, E. P., Hughes,  
631 C. W., & Morrison, A. K. (2015). Recent trends in the Southern Ocean  
632 eddy field. *Journal of Geophysical Research: Oceans*, 120(1), 257-267. doi:  
633 10.1002/2014JC010470
- 634 Hu, S., Sprintall, J., Guan, C., McPhaden, M. J., Wang, F., Hu, D., & Cai,  
635 W. (2020, 2). Deep-reaching acceleration of global mean ocean circula-  
636 tion over the past two decades. *Science Advances*, 6(6), eaax7727. doi:  
637 10.1126/sciadv.aax7727
- 638 Japan Meteorological Agency, Japan. (2013). *Jra-55: Japanese 55-year reanalysis*,  
639 *daily 3-hourly and 6-hourly data*. Boulder CO: Research Data Archive at the Na-  
640 tional Center for Atmospheric Research, Computational and Information Systems  
641 Laboratory. Retrieved from <https://doi.org/10.5065/D6HH6H41>
- 642 Kang, D., & Curchitser, E. N. (2013). Gulf stream eddy characteristics in a high-  
643 resolution ocean model. *Journal of Geophysical Research: Oceans*, 118(9), 4474-  
644 4487. Retrieved from <https://agupubs.onlinelibrary.wiley.com/doi/abs/10.1002/jgrc.20318> doi: <https://doi.org/10.1002/jgrc.20318>
- 645 Kang, D., & Curchitser, E. N. (2017). On the Evaluation of Seasonal Variability of  
646 the Ocean Kinetic Energy. *Geophysical Research Letters*, 47, 1675-1583. doi: 10  
647 .1175/JPO-D-17-0063.1
- 648 Li, G., Cheng, L., Zhu, J., Trenberth, K. E., Mann, M. E., & Abraham, J. P. (2020).

- 650 Increasing ocean stratification over the past half-century. *Nature Climate Change*,  
651 1–8. doi: 10.1038/s41558-020-00918-2
- 652 Martínez-Moreno, J., Hogg, A. M., England, M., Constantinou, N. C., Kiss, A. E.,  
653 & Morrison, A. K. (2021). Global changes in oceanic mesoscale currents over the  
654 satellite altimetry record. *Journal of Advances in Modeling Earth Systems*, 0(ja).  
655 doi: 10.1029/2019MS001769
- 656 Martínez-Moreno, J., Hogg, A. M., Kiss, A. E., Constantinou, N. C., & Morrison,  
657 A. K. (2019). Kinetic energy of eddy-like features from sea surface altime-  
658 try. *Journal of Advances in Modeling Earth Systems*, 11(10), 3090–3105. doi:  
659 10.1029/2019MS001769
- 660 Patel, R. S., Llort, J., Strutton, P. G., Phillips, H. E., Moreau, S., Pardo, P. C.,  
661 & Lenton, A. (2020). The Biogeochemical Structure of Southern Ocean  
662 Mesoscale Eddies. *Journal of Geophysical Research: Oceans*, 125(8). doi:  
663 10.1029/2020jc016115
- 664 Pilo, G. S., Mata, M. M., & Azevedo, J. L. L. (2015). Eddy surface properties and  
665 propagation at Southern Hemisphere western boundary current systems. *Ocean  
666 Science*, 11(4), 629–641. doi: 10.5194/os-11-629-2015
- 667 Qiu, B. (1999). Seasonal Eddy Field Modulation of the North Pacific Subtropical  
668 Countercurrent: TOPEX/Poseidon Observations and Theory. *Journal of Physical  
669 Oceanography*, 29(10), 2471–2486. doi: 10.1175/1520-0485(1999)029<2471:sefmot>2  
670 .0.co;2
- 671 Qiu, B., & Chen, S. (2004). Seasonal Modulations in the Eddy Field of the South  
672 Pacific Ocean. *Journal of Physical Oceanography*, 34(7), 1515–1527. doi: 10.1175/  
673 1520-0485(2004)034<1515:smitef>2.0.co;2
- 674 Qiu, B., Chen, S., Klein, P., Sasaki, H., & Sasai, Y. (2014). Seasonal Mesoscale  
675 and Submesoscale Eddy Variability along the North Pacific Subtropical Coun-  
676 tercurrent. *Journal of Physical Oceanography*, 44(12), 3079–3098. doi:  
677 10.1175/JPO-D-14-0071.1
- 678 Ruela, R., Sousa, M. C., deCastro, M., & Dias, J. M. (2020). Global and regional  
679 evolution of sea surface temperature under climate change. *Global and Planetary  
680 Change*, 190, 103190. doi: 10.1016/j.gloplacha.2020.103190
- 681 Sasaki, H., Klein, P., Qiu, B., & Sasai, Y. (2014). Impact of oceanic-scale inter-  
682 actions on the seasonal modulation of ocean dynamics by the atmosphere. *Nature*

- 683        *Communications*, 5(1), 5636. doi: 10.1038/ncomms6636
- 684        Schubert, R., Schwarzkopf, F. U., Baschek, B., & Biastoch, A. (2019). Submesoscale  
685        Impacts on Mesoscale Agulhas Dynamics. *Journal of Advances in Modeling Earth  
686        Systems*, 11(8), 2745–2767. doi: 10.1029/2019ms001724
- 687        Siegel, D., Peterson, P., DJ, M., Maritorena, S., & Nelson, N. (2011). Bio-optical  
688        footprints created by mesoscale eddies in the Sargasso Sea. *Geophysical Research  
689        Letters*, 38(13), n/a-n/a. doi: 10.1029/2011GL047660
- 690        Uchida, T., Abernathey, R., & Smith, S. (2017). Seasonality of eddy kinetic energy  
691        in an eddy permitting global climate model. *Ocean Modelling*, 118, 41-58. doi: 10  
692        .1016/j.ocemod.2017.08.006
- 693        Wunsch, C. (2020). Is The Ocean Speeding Up? Ocean Surface Energy Trends.  
694        *Journal of Physical Oceanography*, 50(11), 1–45. doi: 10.1175/jpo-d-20-0082.1
- 695        Wunsch, C., & Ferrari, R. (2004). Vertical mixing, energy, and the general circulation  
696        of the oceans. *Annual Review of Fluid Mechanics*, 36(1), 281–314. doi: 10  
697        .1146/annurev.fluid.36.050802.122121
- 698        Wyrtki, K., Magaard, L., & Hager, J. (1976). Eddy energy in the oceans. *Journal of  
699        Geophysical Research*, 81(15), 2641-2646. doi: 10.1029/JC081i015p02641
- 700        Yue, S., & Wang, C. (2004). The Mann-Kendall Test Modified by Effective Sample  
701        Size to Detect Trend in Serially Correlated Hydrological Series. *Water Resources  
702        Management*, 18(3), 201–218. doi: 10.1023/b:warm.0000043140.61082.60
- 703        Zamudio, L., Hurlbert, H. E., Metzger, E. J., Morey, S. L., O'Brien, J. J., Tilburg,  
704        C., & Zavala-Hidalgo, J. (2006). Interannual variability of Tehuantepec ed-  
705        dies. *Journal of Geophysical Research: Oceans (1978–2012)*, 111(C5). doi:  
706        10.1029/2005JC003182